

## An adaptive machine learning approach to improve automatic iceberg detection from SAR images



Mauro M. Barbat<sup>a,\*</sup>, Christine Wesche<sup>c</sup>, Adriano V. Werhli<sup>b</sup>, Mauricio M. Mata<sup>a</sup>

<sup>a</sup> Institute of Oceanography, Federal University of Rio Grande-FURG, Rio Grande, RS 96203-900, Brazil

<sup>b</sup> Computer Science Centre, Federal University of Rio Grande-FURG, Rio Grande, RS 96203-900, Brazil

<sup>c</sup> Alfred Wegener Institute for Polar and Marine Research-AWI, Bremerhaven 27570, Germany

### ARTICLE INFO

**Keywords:**  
Icebergs  
Detection  
SAR  
Southern Ocean  
Machine learning

### ABSTRACT

Iceberg distribution, dispersion and melting patterns are fundamental aspects in the balance of heat and freshwater in the Southern Ocean; yet these features are not fully understood. This lack of understanding is, in part, due to the difficulties in accurately identifying icebergs in different environmental conditions. To improve the understanding, reliable iceberg detection tools are necessary to achieve a detailed picture of iceberg drift and disintegration patterns, and thus to gain further information on the freshwater input into the Southern Ocean. Here, we present an accurate automatic large-scale iceberg detection method using an alternative machine learning architecture applied to high resolution Synthetic Aperture Radar (SAR) images. Our method is based on the concept of adaptability and focuses on improving the performance of identifying icebergs in ambiguous environmental contexts with wide radiometric, textural, size and shape variability. The fundamentals of the method are centred on superpixel segmentation, ensemble learning and incremental learning. The method is applied to a dataset containing 586 ENVISAT Advanced SAR images acquired during 2003–2005 (Weddell Sea region) and to the Radarsat-1 Antarctic Mapping Project (RAMP) mosaic, covering the Antarctic wide near-coastal zone. These images cover scenes under heterogeneous backscattering signatures for all seasons with variable meteorological, oceanographic and acquisition parameters (e.g. band, polarization). Our method is highly adaptable to distinguish icebergs from ambiguous objects hidden in the images. The average false positive rate and miss rate are  $2.3 \pm 0.4\%$  and  $3.3 \pm 0.4\%$ , respectively. Overall, 9512 icebergs with sizes varying from 0.1 to 4567.82 km<sup>2</sup> are detected with average classification accuracy of  $97.5 \pm 0.6\%$ . The results confirm that the method presented here is robust for widespread iceberg detection in the Antarctic seas.

### 1. Introduction

Glacial ice fragments, from few meters (growler, bergy bit) up to dozens of kilometres (Jackson and Apel, 2005, pp. 411; Williams et al., 1999), are able to drift away from their region of origin, subject to fractures and gradual melting associated with water temperature, wave action, ocean currents and wind regime (Bigg et al., 1997; Gladstone et al., 2001). Starting from 15 m length, those fragments are known as icebergs (Jackson and Apel, 2005, pp. 411) and can cause substantial impacts on the global climate and ocean dynamics and circulation. The freshwater flux from iceberg melting plays an important role in disrupting temperature and salinity patterns (Schodlok et al., 2006; Romanov et al., 2008; Stern et al., 2016) and may affect the ocean's biological activity, carbon uptake, sea-ice, ocean circulation and deep-water formation (Silva and Bigg, 2005; Silva et al., 2006; Schodlok

et al., 2006; Schwarz and Schodlok, 2009; Shaw et al., 2011; Stern et al., 2016). However, little is known about icebergs' individual trajectories and the amount of freshwater exported to the open ocean due to their melting (Silva and Bigg, 2005; Mazur et al., 2017). There are relevant studies on the icebergs trajectories (e.g. Schodlok et al., 2006; Jansen et al., 2007; Bouhier et al., 2018), but those are limited to single icebergs or small regions of the Southern Ocean. One of the main issues regarding Southern Ocean observational, modelling, and remote sensing efforts is related to the complexity of identification and monitoring of icebergs (e.g. Jacka and Giles, 2007; Romanov et al., 2012; Wesche and Dierking, 2012; Stern et al., 2016). Satellite data, such as Synthetic Aperture Radar (SAR) images, are derived from an active principle of emission of microwaves and have advantages to avoid contamination from the dense clouds that are ubiquitous in the polar seas. SAR technique is capable of penetrating the dense polar atmosphere under

\* Corresponding author.

E-mail address: [maurobarbat@furg.br](mailto:maurobarbat@furg.br) (M.M. Barbat).

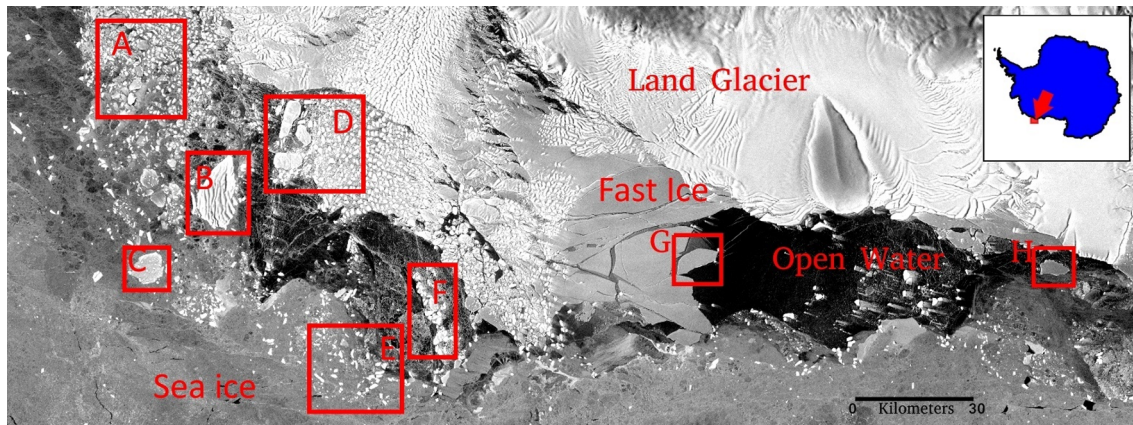


**Fig. 1.** Example of a SAR scene with large spectral, textural and morphological variability. [Rectangles A, D, E, F] give examples of clusters of small icebergs surrounded by ice-melange (mix of iceberg, snow and sea ice) and sea ice, presenting low intensity contrast and lacking boundary definition. Rectangles [B, C] give an examples of iceberg spectral (grey level intensity), textural and morphological heterogeneity, and [G, H] give an examples of drifting fast ice and free sea ice with similar dark iceberg radar signature.

adverse weather conditions even at night (Marino et al., 2016). Furthermore, SAR data provide high spatial and temporal coverage on Antarctica since 1991 and has become a standard dataset for iceberg, glaciers and sea ice research.

Although SAR products provide a useful tool to study the polar environment, in most cases the iceberg signatures in those radar-derived images are not unambiguous with respect to the background. Oscillations in backscatter intensity, attributed to weather conditions, sea state and the presence of sea ice, rough water, and snow-covered islands, can produce similar and ambiguous signatures between icebergs and their surroundings. Fig. 1 shows a typical example of SAR images where variable features coexist in the same image. Rectangles A, D, E, F in Fig. 1 give examples of clusters of small icebergs surrounded by ice-melange (mix of iceberg, snow and sea ice) and sea ice, presenting low intensity (signal) contrast, hence lacking sharp boundary definition. Rectangles B, C, D give examples of iceberg spectral (gray-level intensity), textural and morphological heterogeneity, and G, H give examples of drifting multiyear fast ice with similar radar signature compared to darker icebergs. Therefore, icebergs have high likelihood to be mistakenly identified from other coexisting features in SAR images. This makes an accurate identification of icebergs in SAR images a complex, challenging and necessary task. To our best knowledge, the differentiation of icebergs from other features in SAR images has relied for a long time on empirical relationships of surface and backscatter intensity expressed by probability density functions, essentially applying linear models to separate icebergs from the background (e.g. Williams et al., 1999; Silva and Bigg, 2005; Wesche and Dierking, 2012). Many studies on iceberg detection using SAR imagery were published in the last decades and we briefly highlight only the most relevant to the present study. Williams et al. (1999) focused on edge detection using image texture and contrast properties, followed by a pixel bonding segmentation to separate icebergs from the background. The differences between the backscattering intensities of icebergs and their surroundings were used by Silva and Bigg (2005) and Wesche and Dierking (2012). The method presented by Frost et al (2016) uses a Constant False Alarm Rate (CFAR) by constantly computing false alarm probabilities based on the assumption given by the user about expected probability density function of the backscatter intensity in the observed region. Methods using polarimetric SAR data have also been tested (Marino et al., 2015, 2016). Nevertheless, polarimetric data are very limited in availability and spatial coverage. In a recent study, Mazur et al. (2017) developed a method based on brightness and spatial parameters computed from five scale levels of segmentation in that area.

Nevertheless, all these methods rely on empirical relations of the

backscatter intensities which can be violated in different situations (Wesche and Dierking, 2015). This limitation constrains the use of a reliable screening procedure that performs iceberg identification automatically and universally. Hours of visual inspection appears to be the only way to improve detection performance, so an accurate automatic iceberg detection method is a demanding and necessary tool for many applications.

In general, accurate iceberg identification relies on the performance of distinguishing icebergs from open water or sea ice under different meteorological, sea state or iceberg surface conditions. These conditions result in substantial variations from highly bright to dark objects shown in the derived images. This variable spectral behaviour along with changing textural and morphological patterns makes it difficult to establish a general predictive model applicable to differentiate icebergs from coexisting features in SAR images, hence supporting the need for adaptive approaches.

In this sense, we propose an alternative pixel-based machine learning architecture, which employs an intuitive solution to address the aforementioned problem. Essentially, the method relies on using the predictions derived from different models based on various image properties, instead of using output from only one model. As the main result of this approach, the ability to predict multi-modal objects is strongly improved, thus reducing the instability of individual classifiers and increasing versatility to adapt to new samples, even outliers.

In the subsequent sections, we present the dataset used in this study and describe the proposed machine learning architecture and performance evaluation metrics, followed by the results and a thorough performance evaluation of the method. The final two sections bring a detailed discussion of the results and the conclusions, which summarize and complete this study.

## 2. Data

We introduced two distinct datasets to evaluate the performance of our proposed method. The first dataset is the 586 Envisat ASAR (Advanced Synthetic Aperture Radar) WSM (Wide Swath Mode – 400 km wide range) medium resolution (pixel size 75 m × 75 m) images (ASA\_WSM\_1P), acquired at C-Band (5.3 GHz, wave length ~5.6 cm) and HH polarization (ESA, 2007) during 2003–2005. The main observation area is the Weddell Sea (centred at 70°S, 45°W) for all seasons. The second dataset is the RAMP AMM-1 amplitude mosaic, constructed from over 3000 individual frames acquired by the Canadian Radarsat-1 in C-Band at a pixel size of 25 m × 25 m (resampled onto 100 m × 100 m resolution) during September–October of 1997 for the Antarctic wide near-coastal zone (Jezek et al., 1998). All images

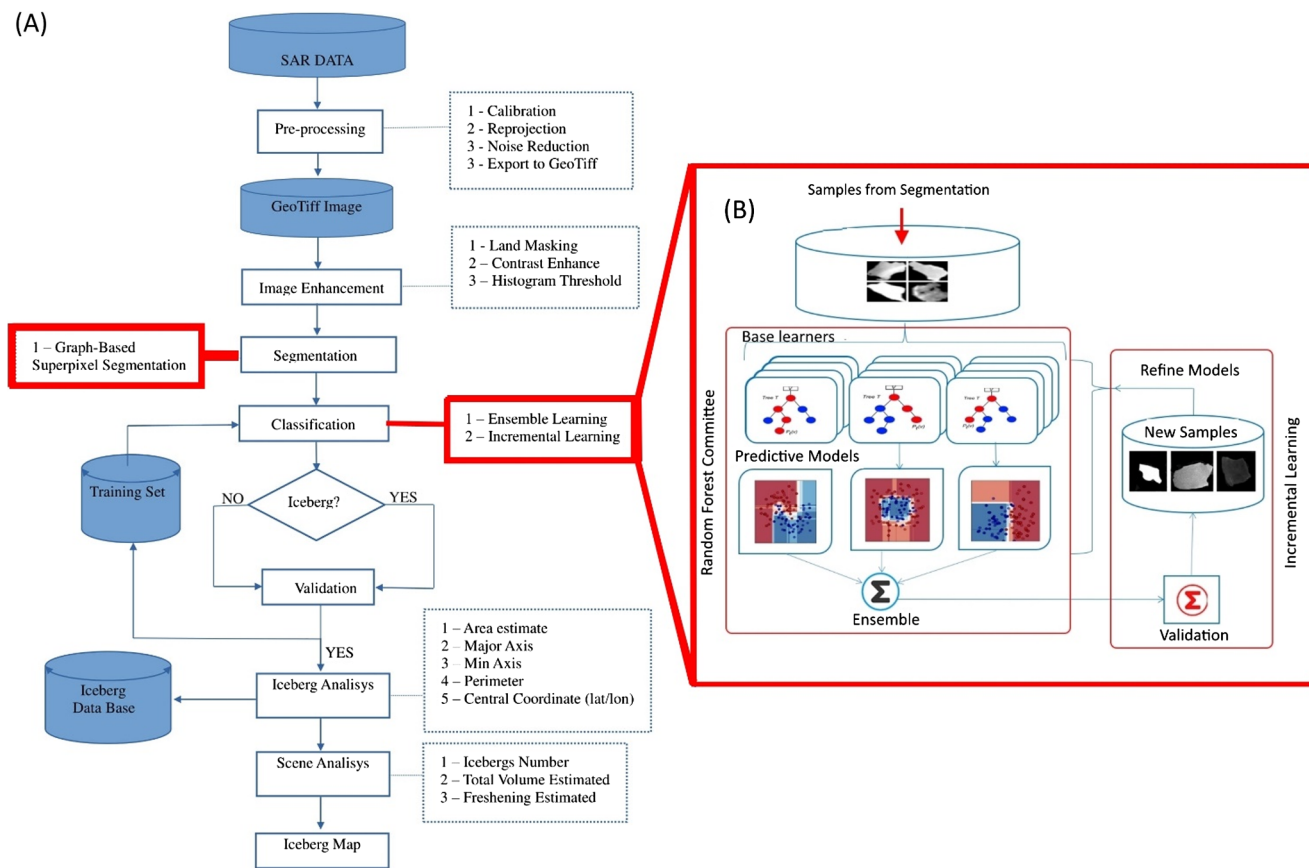


**Fig. 2.** Overview of the proposed detection method architecture. Panel (A) shows an overview of the detection framework. The red rectangles highlight the superpixel segmentation, ensemble learning and incremental learning stages. Panel (B) is a zoom-in in the classification stage disclosing the machine learning architecture, exposing ensemble learning and incremental learning. (For interpretation of the references to colour in this figure legend, the reader is referred to the web version of this article.)

were (i) calibrated (each pixel intensity (grayscale) can be directly related to the radar backscatter strength; Rosich and Meadows, 2004), (ii) re-projected onto EPSG:3031 WGS 84/Antarctic Polar Stereographic projection (Latitude of origin –90°, Central meridian 0°, Standard parallel –71°), (iii) speckle reduced with a Lee-Sigma filter (Lee, 1981; Lee, 1983), (iv) land data removed, and (v) converted into 8-bit unsigned integer Geotiff images. Both datasets add up to approximately 7 TByte of data storage.

### 3. Method

Our proposed method is based on the grid-graph-based superpixel segmentation (Felzenszwalb and Huttenlocher, 2004), ensemble learning (Zhou, 2012) and incremental learning (Polikar, 2006). An overview of our method is presented in Fig. 2, where we show of the main characteristics of our architecture and the roles of the three backbone methodologies cited above. Further details will be explained in the following subsections. In order to individualize the different objects that are present in the scenes, the graph-based superpixel segmentation captures redundancies by reducing the high resolution pixel space to a set of meaningful homogeneous regions. It also preserves details in low-variability image regions, while ignoring details in high-variability regions. Random Forest Committee is an ensemble learning method that uses a set of Random Forest classifiers (Breiman, 2001) as base learner, based on different arrangements of image features. Polikar's (2006) incremental learning improves the distinct predictive models by the incremental addition of new samples and refines the models continuously rather than having a one-shot training phase.

### 3.1. Segmentation

The detection of icebergs in SAR imagery requires a separation of each individual iceberg and a reliable description of the backscattering behaviour of each object using the image features. Superpixel algorithms are capable to capture image redundancies and group single pixels into perceptually meaningful atomic regions (Achanta et al., 2011). It provides a convenient basis to compute image features, spatial properties and reduces the complexity of subsequent image processing tasks by decreasing the rigid pixel grid structure to a set of atomic regions (Achanta et al., 2010; Zhang et al., 2017).

There are different variants of superpixel segmentation algorithms (e.g. Comaniciu and Meer, 2002; Felzenszwalb and Huttenlocher, 2004; Veldadi and Soatto, 2008; Achanta et al., 2010). Operationally, we particularly aim to individualize possible icebergs in SAR images under such conditions: (i) icebergs can appear partially connected to one or more objects, (ii) plausible icebergs present very low contrast to the background, (iii) icebergs can appear in a wide range of sizes and (iv) adherence to iceberg boundaries is of paramount importance to allow to compute spatial metadata. In this sense, we conducted a series of experiments to evaluate computational efficiency and the performance of preserving shape details in complex targets. We found that the graph-based segmentation proposed by Felzenszwalb and Huttenlocher (2004) has the best performance for our task. In practice, the superpixel graph-based method performs simple greedy decisions based on three parameters (settings used in this study are within parentheses): (i) scale – sets the observation level, higher means less and bigger segments (50); (ii) sigma – performs a median filter over the image (0); and (iii) minimal size – minimum number of pixels to create a single segment

(10). The goal is to produce a cluster of pixels as nodes on a graph. Each node (segment) is recursively adjusted considering a minimum distance ( $L$ ), defined as  $L(v_i, v_j) = |I(p_i) - I(p_j)|$ , where  $L(v_i, v_j)$  is the edge distance between the nodes  $v_i$  and  $v_j$ .  $I(p_i) - I(p_j)$  is the Euclidean distance, in terms of pixel intensity, between each pixel inside the node and its neighborhood. The number of detected segments is directly associated to the image contrast and can be indirectly controlled by the scale parameter. For more information on the segmentation technique used here it is referred to [Felzenswalb and Huttenlocher \(2004\)](#).

After the initial segmentation, usually large icebergs with a wide horizontal area can present a wide textural gradient resulting in over segmentation (segments inside bigger segments). To reduce these inconsistencies, we gradually merge the similar segments hierarchically using the Region Adjacency Graph (RAG) technique ([Tremblay and Colantoni, 2000](#)), applying an intensity distance threshold of 15% defined by several tests. This produces superpixels that adhere well to the limits of icebergs, even if they have irregular geometry and/or large surface texture gradient. It also allows us to estimate the iceberg area based on the superpixel spatial properties as:

$$\text{area}_{\text{km}^2} = \left( \left( \text{sp\_area}_{\text{pixels}} - \left( \frac{\text{sp\_perimeter}_{\text{pixels}}}{2} \right) \right) \times \text{pixelSize}_{\text{m}^2} \right) \times 10^{-6} \quad (1)$$

where  $\text{sp\_area}$  is the superpixel horizontal area and  $\text{sp\_perimeter}$  is the superpixel perimeter size. Half of the perimeter size is removed since those pixels define the bordering area between iceberg and its surroundings. [Fig. 3](#) shows an example of segmentation applying [Felzenswalb and Huttenlocher \(2004\)](#) method on a SAR image (panel A) where the red lines in panel (B) define the segmentation boundaries. It is possible to observe the adherence of the segments boundaries to the shape of the different objects present in the image, panel (C) shows a detailed view in icebergs segmented by the method.

### 3.2. Image features selection

Variations of backscattering signatures from icebergs, sea ice and open water surface caused by environmental conditions often result in objects with wide radiometric variability. The radar backscattering coefficient ( $\sigma^0$ ) of an iceberg is the sum of surface and volume contributions ([Wesche and Dierking, 2012](#)). The surface of icebergs can be

covered by snow, firn and/or melt ponds. Additionally, icebergs can roll over, in such case exposing their surface as pure glacial ice, frequently not exhibiting a positive contrast compared to the background. In regions, where the air temperatures are above the melting point, liquid water and/or wet snow on the iceberg surface reduces the volume scattering, resulting in “dark” icebergs ([Wesche and Dierking, 2012](#)). Wind roughened open water can have very high backscatter intensity which depends on the wind direction relative to the radar imaging direction ([Williams et al., 1999](#)). The backscatter intensity from sea ice increases as it is broken into small floes or it is low-salinity multi-year sea ice ([Williams et al., 1999; Gladstone and Bigg, 2002; Muckenhuber et al., 2016](#)).

Analysing the main variations observed in icebergs and their background from the SAR images, we determined 32 image features for iceberg detection. The aim is to compute a set of image features capable to describe icebergs and background from distinct perspectives. Here, we give a brief overview on the features applied. In addition, [Appendix A](#) provides further details on the formal definition of each of those features (with the exception of basic statistics).

- Five statistical spectral variables (mean, standard deviation, median, mode and energy) are used. They are based on pixel intensity derived from the backscatter coefficient ( $\sigma^0$ ), which is the most common parameter describing icebergs ([Williams et al., 1999; Gladstone and Bigg, 2002; Wesche and Dierking, 2012; Mazur et al., 2017](#)).
- Seven histogram-based statistical moments (mean, variance, skewness, kurtosis, entropy, mode and slope) are used. They are derived from observing the histogram of an image. They can be specified independently of any real image content by a discrete probability distribution ([Blachnik and Laaksonen, 2008](#)). Moreover, these moment parameters are powerful tools to analyse spatial texture characteristics ([Chen et al., 2003; Singh and Singh, 2002](#)).
- Two frequency texture features (mean and variance) are used. They are based on a wavelet-based Gabor filter, extracting fine texture measures with translation, rotation, illumination and scale invariance from the spectral energy patterns ([Masotti and Campanini, 2008; Mishra et al., 2010; Ismail et al., 2014](#)).
- Twelve texture measures are derived from three parameters (contrast, homogeneity and dissimilarity) per angle ( $0^\circ$ ,  $45^\circ$ ,  $90^\circ$  and

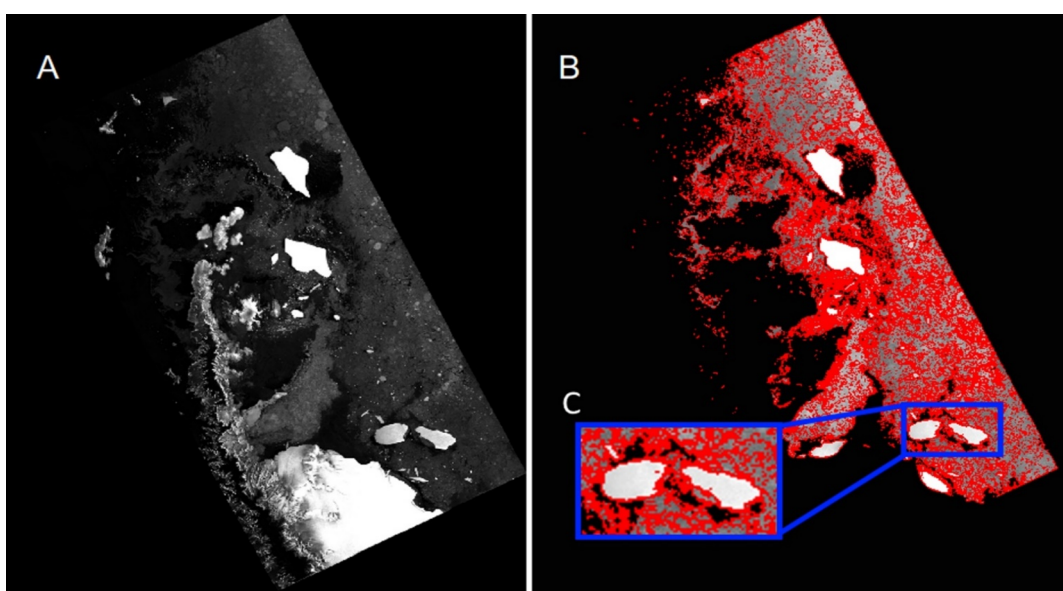


**Fig. 3.** Segmentation applying [Felzenswalb and Huttenlocher \(2004\)](#) method to a SAR image (panel A). Red lines (panel B) defines the segmentation boundaries. Panel (C) zoom in icebergs segmented by the method. (For interpretation of the references to colour in this figure legend, the reader is referred to the web version of this article.)

135°). They are based on the Grey Level Co-occurrence Matrix (GLCM) proposed by Haralick et al. (1973). It is an useful method to provide statistics about texture patterns. Essentially, it counts how many combinations of different grey levels occur in the image in different angles;

- Six morphological features are used. They are based on superpixel shape (i) eccentricity – the ratio of the distance between the two focal points of an ellipse that has the same second-moments as the superpixel region, (ii) equivalent diameter to a circle that has the same area as the superpixel region (roundness), (iii) ratio of pixels in the superpixel to pixels of the convex hull (solidity), (iv) compactness degree (Polsby-Popper test (Polsby and Popper, 1991)), (v) normalized perimeter index, and (vi) fractal dimension (De Keersmaecker et al., 2003).

### 3.3. Ensemble learning

For automatic detection systems, the diversity of objects from the same class causes problems. This is because predictive models (linear or polynomial) usually are not able to separate objects with similar features. In ensemble learning approaches, different predictive models are combined to increase the prediction accuracy, reducing the instability of individual classifiers (Dietterich, 2000). In contrast to ordinary learning approaches, diversity is a fundamental issue in improving the ensemble methods (Zhou, 2012). Intuitively, it is understandable that the individual predictive models must be different to gain from combination. In cases where the hypotheses space is too large to explore, several different hypotheses reduce the risk of choosing the wrong one. Diversity can be achieved with distinct approaches, e.g. manipulating the training samples to generate multiple hypotheses (bagging/bootstrap), training each classifier with a random subset of the training set (Breiman, 2001) or manipulating the input features so that each classifier is trained with a subset of the features space (Eibl and Pfeiffer, 2005). Fig. 4 shows an example of decision boundaries applied over ambiguous objects (adapted from Zhou, 2012).

Among the classic ensemble classifiers, the non-linear and non-parametric Random Forest (RF) algorithm proposed by Breiman (2001) has been gaining attention and has been widely investigated and applied to distinct problems (Beard, 2007; Özçift, 2011; Hayes et al., 2014; Ghosh et al., 2014; Puissant et al., 2014; Du et al., 2015). The RF algorithm has the following advantages: (i) its efficiency allows the prediction of inputs of different natures (Ghosh et al., 2014), (ii) it presents high computational performance (Gislason et al., 2006; Du et al., 2015), (iii) it allows a feature measure importance, (iv) it is less sensitive to the quality of training samples and noise (Puissant et al.,

**Table 1**

Feature representability ranked by information gain. Computed by Correlation-based Feature Selection (CFS). 0 means no relevance and 1.0 maximum relevance.

Name	Feature Domain	CFS
GLCM 0 Contrast	Texture	0.563
GLCM 180 Contrast	Texture	0.539
Equivalent diameter	Morphology	0.530
Fractal Dimension	Morphology	0.509
Polsby-Popper	Morphology	0.498
GLCM 270 Contrast	Texture	0.471
Spectral STD	Intensity	0.437
GLCM 90 Contrast	Texture	0.424
Histogram Mean	Texture	0.417
Histogram skewness	Texture	0.417
Histogram kurtosis	Texture	0.414
Histogram Slope	Texture	0.396

2014), (v) it is robust to outliers and overfitting, even if the number of trees is increased in the forest (Özçift, 2011), and (vi) it is suitable to problems where the dimensionality and highly correlated data pose major challenges to other classification methodologies (Belgiu and Dragu, 2016).

In the method proposed here, we constructed a meta-ensemble (an ensemble of ensemble classifiers) approach, where a RF Committee is created from the combination of a set of heterogeneous RF base classifiers, as illustrated in Fig. 2. The committee is defined by five base learners, (i) CFS-RF, using the twelve most representative image features defined by Correlation-based Feature Selection (CFS) (Hall, 1999), presented in Table 1; (ii) Morpho-RF based on morphological features; (iii) GLCM-RF, specialist in textural variation in different angles; (iv) HistoGabor-RF specialist in textural properties in space and frequency domain, using histogram statistics and Gabor features; and (v) Spectral-RF, specialist on statistical intensity features, derived from the radar backscatter intensity.

The predictive result from the RF Committee is built by combining the individual votes from the five RF classifiers used as base learners. Each RF base learner casts a single vote and its associated confidence level, thus indicating the probability with which the vote is true. The applied combination method is defined by the weighted average of the votes (weighted by the confidence level) between the different RF classifiers. The RF committee gives the combined output as:

$$RF(x) = \sum_{i=1}^T w_i h_i(x) \quad (2)$$

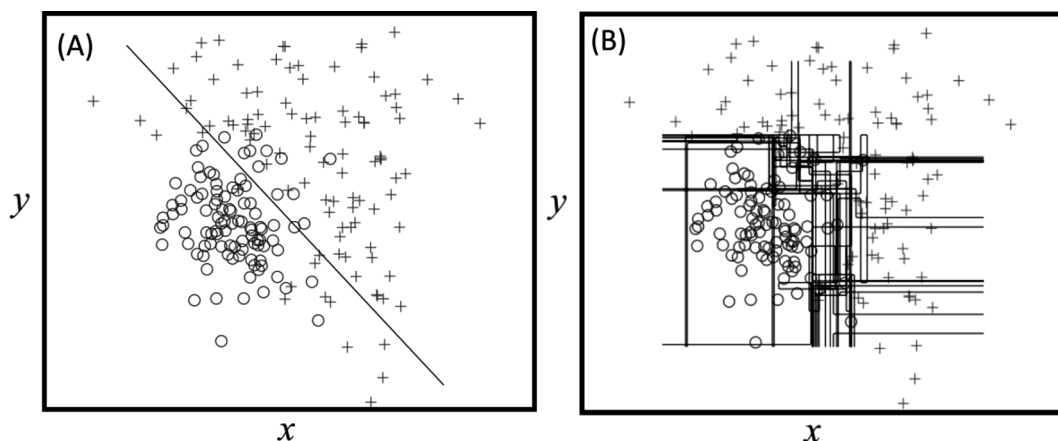


**Fig. 4.** Example of decision boundaries applied over ambiguous objects (adapted from Zhou, 2012). Panel (A) shows a linear predictive model, presenting the classification errors from both targets. Panel (B) shows the RF decision boundaries. Different from linear approaches, the RF is defined through a merge of distinct decision boundaries computed from a set of heterogeneous decision trees based on different arrangements of image features. It results in predictive boundaries which are more flexible, thus leading to a better generalization skill.

where  $w_i$  is the weight for  $h_i$ , and the weights  $w_i$ 's are usually assumed to be constrained by

$$w_i \geq 0 \text{ and } \sum_{i=1}^T w_i = 1 \quad (3)$$

Supposing that the true function capable to separate all objects is  $f(x)$ ,  $x$  is sampled according to a distribution  $p(x)$ , and the output of each base learner can be written as the true value plus an error:

$$h_i(x) = f(x) + \epsilon(x), i = 1, \dots, T \quad (4)$$

The ensemble error for weighted vote can be write as (Perrone and Cooper, 1993):

$$err(RF) = \int \left( \sum_{i=1}^T w_i h_i(x) - f(x) \right)^2 p(x) dx \quad (5)$$

### 3.4. Incremental learning

Supervised learning approaches are widely applied to machine learning problems, due to their performance and flexibility derived from a predictive model using a preconditioned and labelled training set. However, a manually obtained training set is often time expensive, demanding several hours for an expert to provide diversified instances capable of fitting an accurate predictive model.

Icebergs and background elements from SAR images usually contain different scales of variability and signatures. It results in a wide range of image patterns which is not usually contemplated by the training set. Therefore, we adopted an incremental learning approach known as batch learning mainly due to its versatility and performance to adapt to new samples introduced dynamically to the training set. In this way, new validated (high confidence levels from all committee members) samples are gradually merged into a training set automatically, adapting the predictive models to new samples subsequently (Impoco and Tuminello, 2015). In practice, the proposed learning approach starts with an initial hypothesis from all base learners given by an initial manually derived training set containing 100 instances (50 icebergs and 50 non-iceberg samples). In the following steps, iceberg and background elements that have been classified in previous rounds are used as reference to label new samples. Gradually, an evaluation operator receives feedback from further new samples and checks the candidate to the new model applying a cross-validation. If the model accuracy and precision increase, the new model is used. In this way, the wide variability captured by SAR images is added into the training set dynamically, allowing the same training set to be used on different SAR datasets with high performance. The full performance of the predictive models can vary depending on the level of variability between distinct datasets, however once the incremental approach starts to receive new samples, performance tends to stabilize.

## 4. Performance analysis

The purpose of the method is to improve the performance of automatic iceberg detection in SAR images under large spectral, textural and morphological variability. Two approaches are used to compute the ensemble/incremental learning performance of iceberg detection in SAR images. First, a visual inspection was performed over five frames with large iceberg density from RAMP AMM-1 mosaic looking for misses and false positives, similar to the approach used by Wesche and Dierking (2015), followed by a comparison of the RF committee performance against the individual classifiers base learner (all using the same training set). We manually set up a test dataset with 1850 samples and computed five machine learning evaluation metrics. Those metrics are achieved by assuming true positives (TP) for correct iceberg, true negatives (TN) for correct non-iceberg, false positives (FP) for incorrect iceberg and false negatives (FN) for incorrect non-iceberg:

**1. Accuracy (ACC):** Returns the rate of correct predictions without differentiating positives from negatives.

$$Accuracy = \frac{TP + TN}{TP + TN + FP + FN} \quad (6)$$

**2. Precision:** Reflects the proportion of predicted positives that are real positives, which is the ratio between the number of icebergs classified correctly and the amount of objects classified as iceberg.

$$Precision = \frac{TP}{TP + FP} \quad (7)$$

**3. Miss rate:** Reflects the probability to miss a positive object, in this case an iceberg.

$$Missrate = 1 - \frac{TP}{TP + FN} \quad (8)$$

**4. False Positive Rate (FPR):** Reflects the probability of false alarms.

$$FPR = 1 - \frac{TN}{TN + FP} \quad (9)$$

**5. Matthews Correlation Coefficient (MCC):** Reports the quality of binary classifications, where 0 indicates random classification and 1 indicates perfect prediction score (Matthews, 1975).

$$MCC = \frac{TP \cdot TN - FP \cdot FN}{\sqrt{(TP + FP)(TP + FN)(TN + FP)(TN + FN)}} \quad (10)$$

## 5. Results and performance evaluation

### 5.1. Segmentation performance

Similar to Williams et al. (1999) and Silva and Bigg (2005), the segmentation performance analysis was carried out by comparing individual segments produced by the superpixel approach with visual interpretation. We selected 250 icebergs bigger than 30 image pixels in order to observe the superpixel adherence to the object shape. In this case study, 234 (93.6%) of the previously selected icebergs produced a solid and well-defined segmentation (when the segment contour fits a single object), robust to bounding objects under both low and high spectral variability. The worst performance was observed in scenes with presence of clusters of icebergs, which were partially connected, and in scenes where large icebergs presented abrupt textural and spectral variability over its surface. In these situations, iceberg clusters were compacted into single segments resulting in over segmentation and/or poorly defined segmentation.

### 5.2. Detection performance by visual inspection

Following the automatic detection, five RAMP AMM-1 frames with large iceberg density were selected. Obvious false positives, mainly objects partially connected to coastline, sea-ice ridges and spots of rough open water were visually counted. In total, 34,321 targets (icebergs and background) were bounded, resulting in 1809 automatically detected icebergs from those five SAR frames. Applying visual inspection, 47 false positives, identified as sea-ice or spots of rough open water, were noted. Also, 63 obvious misses were detected, which were usually icebergs partially connected with one or more icebergs and/or due to segmentation failure. The number of false positives and misses represented 2.6% and 3.5% of the total number of icebergs automatically detected, respectively. However, a considerable number of misses resulted from the presence of small objects < 5 image pixels. The number of misses is partly caused by the minimal area threshold (10 image pixel) used for the automatic iceberg classification. The minimal area threshold was defined in order to allow the computation

**Table 2**

Total number of objects (icebergs and background elements) bounded by the segmentation stage for each analysed frame. Also, find below the number of automatically detected icebergs and the number of missed and false positives icebergs, which were counted by visual inspection.

	Objects	Icebergs	Miss	False Positive
Frame 1	8163	343	5	7
Frame 2	5480	188	7	4
Frame 3	6966	339	8	11
Frame 4	9840	489	32	13
Frame 5	3872	450	11	12

of textural features and reliable surface intensity statistics. **Table 2** shows the total number of objects (icebergs and background elements) bounded by the segmentation stage for each analysed frame. **Table 2** also shows the number of automatically detected icebergs as well as the number of missed and false positives icebergs, which were counted by visual inspection.

### 5.3. Detection performance by machine learning evaluation

In total, 1850 new balanced samples (icebergs and non-icebergs), showing a wide signature variability, were manually selected to be used as a test set free of errors. This allows a straightforward comparison between the proposed ensemble learning method (RF Committee) and the different base classifiers used. The goal is to monitor the gain from the combination of heterogeneous base classifiers for iceberg detection. Please note that each base classifier is a specialist in a class of image features and all base classifiers are trained to use the same training set through incremental learning.

**Fig. 5** shows the Matthews correlation coefficient (MCC), accuracy (ACC) and precision computed from the RF committee and all base classifiers used. The proposed RF committee achieved an ACC, precision and MCC of 98%, 98% and 95%, respectively.

In general, the RF Committee shows significant improvements in all three parameters (ACC, precision and MCC) when compared to the single base classifiers. The average ACC, precision and MCC showed by the base classifiers are  $88.6 \pm 5\%$ ,  $88.4 \pm 5.4\%$  and  $77.2 \pm 10\%$ , respectively. The major gain from ensemble learning approaches can be better expressed by the false positive and miss rate. To our best

knowledge, even recent methods usually demand manual false positive reduction (Mazur et al., 2017) and manual detection of missed icebergs (Wesche and Dierking, 2015) to improve accurate automatic iceberg detection. These tasks are time expansive, exhausting and not feasible to be applied over large-scale detection as well as for operational near real-time tasks.

A comparison of the false positive and miss rates between the proposed RF Committee and the base classifiers is shown in **Fig. 6**. The RF committee notably outperforms all base classifiers presenting a False Positive Rate (FPR) of 2% and miss rate of 3%. CFS RF, Morpho RF and HistoGabor RF showed a much higher FRPs and miss rates. The adaptive approach proposed in this study results in a high identification rate with low miss and false positive rates, which agrees with the ensemble learning proposal of minimizing misclassification errors (Zhou, 2012). The variability observed between the distinct base learner scores reflects the diversity observed in SAR images. The RF Committee predicts taking advantage of a set of heterogeneous models, rather than trying to find the best model for each situation. The improvement arises from the main problem for iceberg classification variability (i.e. the usual signal ambiguity with the background), in those situations the combination of the distinct models, even limited ones, plays a key role. If we directly compare the precision, the Spectral RF shows a precision of 92%, with a FPR and a miss rate of 7% and 19%, respectively. The RF Committee amounts the precision to 98% and a FPR and miss rate of 2% and 3%, respectively. This improvement is noteworthy and robust, thus reducing the need for manual verification.

### 5.4. Relationship between incremental learning and ensemble learning

The incremental learning approach proposed in this study dynamically introduces batches of new samples into the training set in order to improve the diversity. Since iceberg and background elements show large variability, it is not uncommon to find new objects with outlier characteristics. To evaluate the robustness of the RF Committee to incremental learning, we compared the ACC as a function of the number of training samples, adding manually batches of 100 balanced samples at a time (**Fig. 7**). This ensemble approach shows stable behavior when compared to any of its base classifiers. This behavior is expected, once the ensemble method is robust to outliers and overfitting due to the combination of heterogeneous base learners (Dietterich, 2000; Breiman, 2001; Özçift, 2011). The Spectral RF accuracy (full red line in

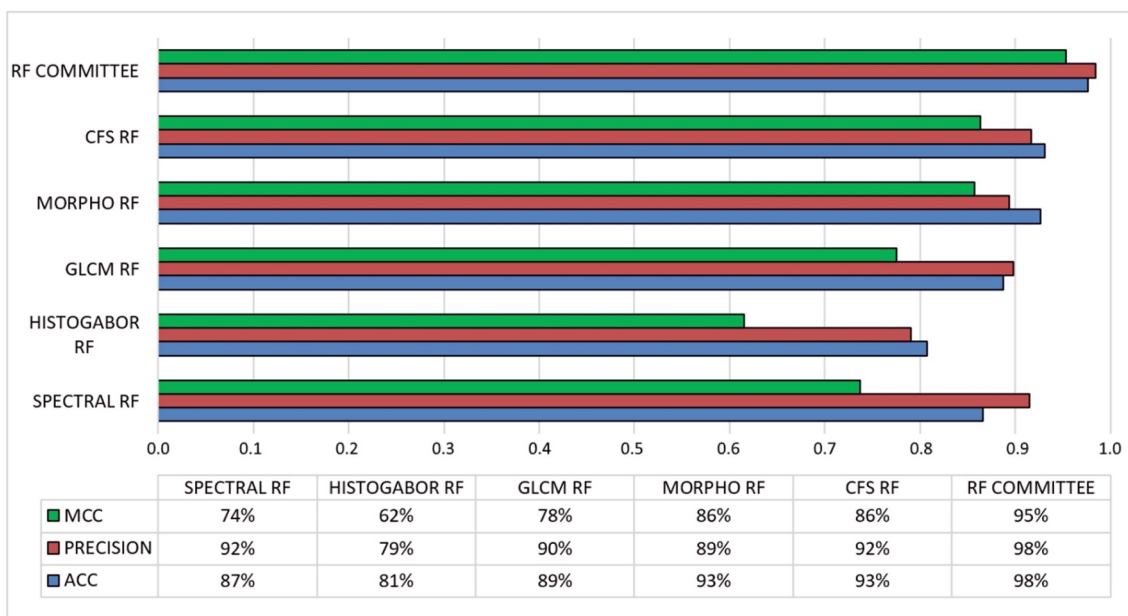


**Fig. 5.** Matthews correlation coefficient (MCC), accuracy (ACC) and precision computed from RF committee and all base learner used.

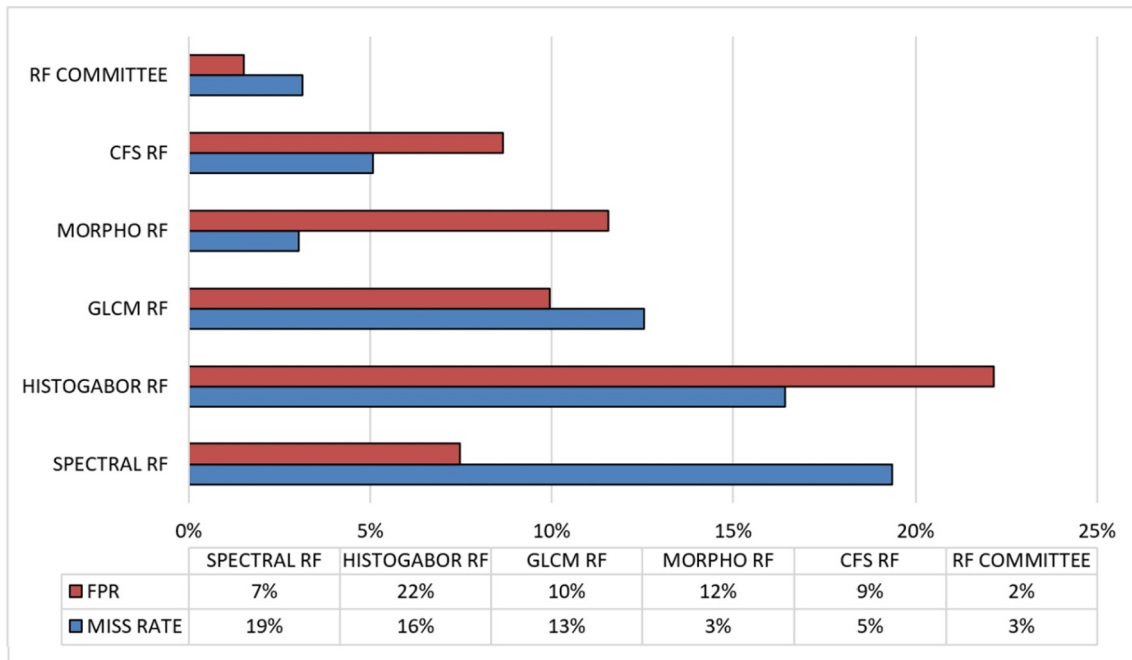


**Fig. 6.** False positive and miss rate comparison between the proposed RF Committee and the base classifiers individually.

Fig. 7) shows a wide variability due to the presence of icebergs with bright and dark signatures. In practice, the strong generalization achieved by the combination of heterogeneous predictive models can be attributed to three fundamental issues: (i) statistical - in cases that the hypothesis space is too large to choose one, diversity can reduce the chance to choose the wrong one, (ii) computational - single learning algorithms can get stuck in the local optima, and (iii) representation - in many cases the true hypothesis could not be represented by any hypothesis individually (Zhou, 2012).

### 5.5. Detection results

Overall, 9512 icebergs were detected with 1863 from the Envisat ASAR dataset and 7649 from RAMP AMM-1 mosaic. Assuming a minimal area threshold of 10 image pixels, it was possible to identify icebergs with areas between 0.1 and 4567.82 km<sup>2</sup> subdivided in five size classes, A1 = 0.1–1 km<sup>2</sup>, A2 = 1–10 km<sup>2</sup>, A3 = 10–100 km<sup>2</sup>, A4 = 100–1000 km<sup>2</sup> and A5 > 1000 km<sup>2</sup>, as proposed by Wesche and Dierking (2015). It is important to note that the total number of icebergs from the Envisat ASAR dataset reflects the actual number of

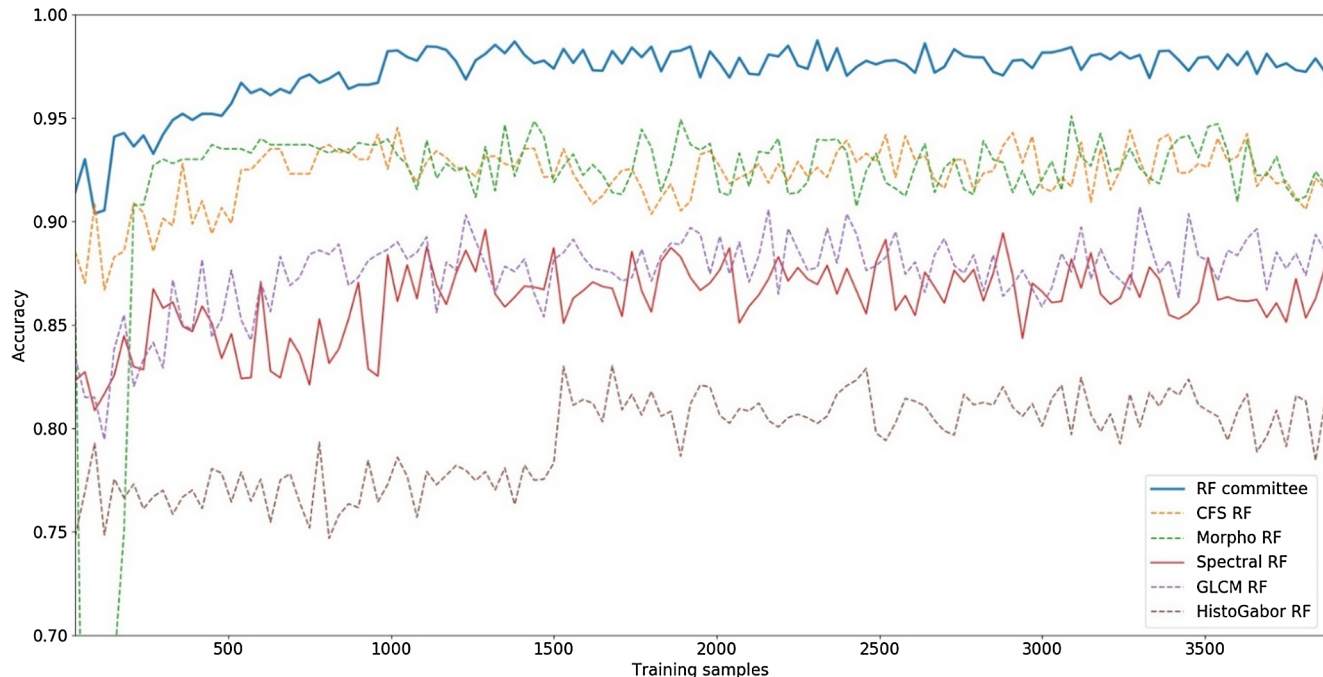


**Fig. 7.** Classification accuracy as function of number of training samples between the proposed RF committee (full blue line) and its distinct base classifiers individually. The full red line highlights Spectral RF accuracy performance. (For interpretation of the references to colour in this figure legend, the reader is referred to the web version of this article.)

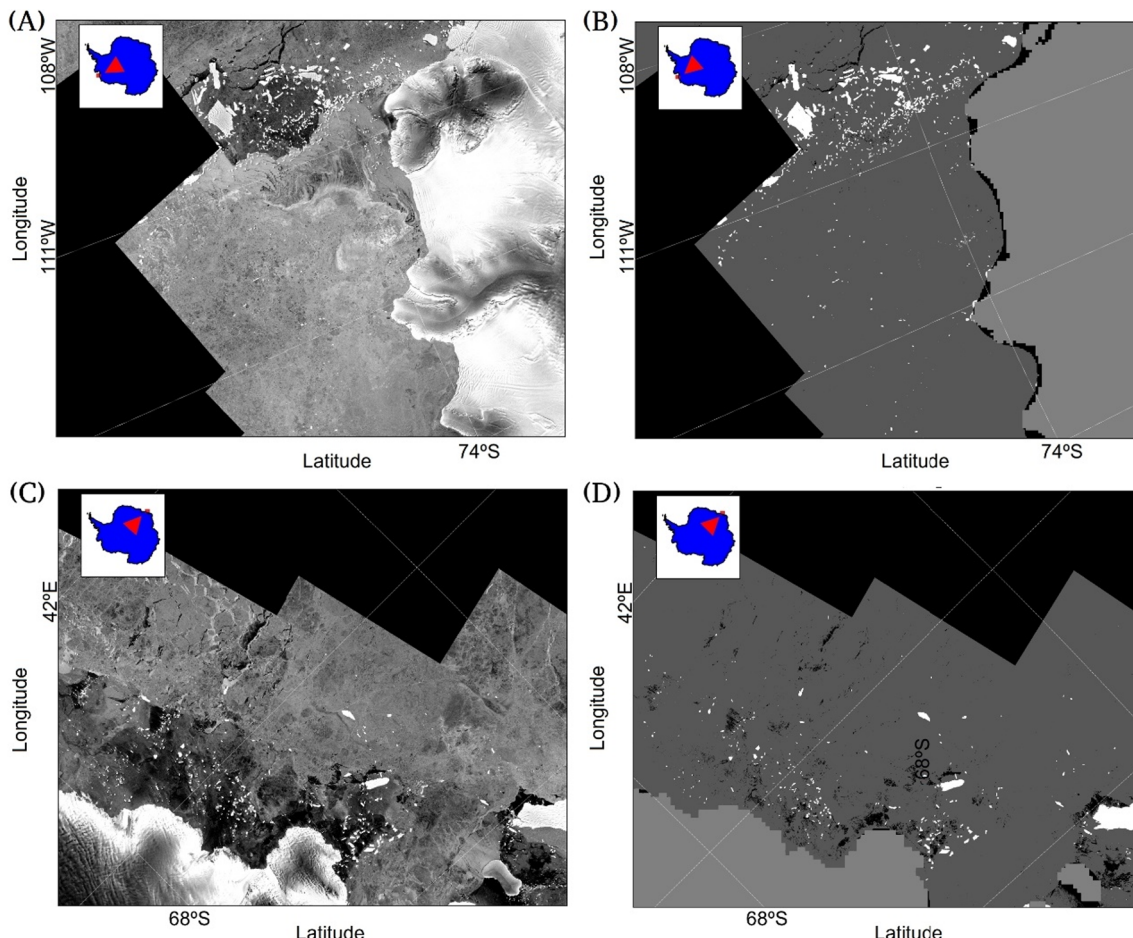


**Fig. 8.** Example of RAMP AMM-1 SAR frames [Panels A and C] used as basis for the classification. Classification results as a mapping product are shown in [Panels B and D]. White objects in B and D are icebergs while light grey shades define the background (e.g. sea ice, open water), dark grey shades define fixed structures (e.g. continental land, ice shelves, ice tongues and glaciers) and black areas represent no-data.

icebergs identified from all images, which contain recurrences. These recurrences are due to overlapping images from different satellite orbits. Another factor contributing to the recurrences is due the wide imaging range in wide swath mode (400 km), the time span of the ENVISAT images and the iceberg mobility. Also, we cannot discard recurrences from the RAMP AMM-1 dataset, however in this case the mosaic is generated from images spanning ~1.5 months, in which case the major part of the recurrences were restricted to class A1 icebergs. Fig. 8 shows examples of RAMP AMM-1 SAR frames [Panels A and C] used as basis for the classification. Classification results are shown in [Panels B and D]. Both SAR frames show complex targets with wide gray-level intensity, textural, size and shape variability.

A summary of the size class distribution (with recurrence effect removed) of icebergs detected in this study is presented in Fig. 9. The total number of individual icebergs is 8064. Class A1 has the largest number in our detection scheme and occupies ~69% in our datasets. The most icebergs class A3, A4 and A5 detected come from the Envisat dataset, which is restricted to the Weddell Sea. We point out that, although the estimated sizes are realistic and reasonable, possible biases towards the size estimates should be considered. It is not uncommon that small fragments of iceberg do not present a robust scattering signal or extra pixels signatures distinct from very bright sea ice, which eventually is found attached to those fragments.

The spatial and size distribution from all detected icebergs is shown in Fig. 10. The high concentration close to the coast is due to the geographic limitations of the RAMP AMM-1 mosaic, since this mosaic was developed for continental studies (Jezek et al., 1998). In terms of

detection, the spatial restriction allows us to perform a classification under high diversity of sea-ice coverage, one of the main obstacles in standard iceberg classification methods. In order to perform a detection in open sea and in different seasons, the ENVISAT ASAR dataset was used (thus restricted to Weddell Sea).

No significant seasonal variability related to the method performance was observed. Nevertheless, the number of detected icebergs is higher in winter and spring than in summer and autumn. As described by Wesche and Dierking (2012), the winter season appears to be more suitable for iceberg identification since the environmental conditions (air temperature, presence of smooth new sea ice) foster the contrast between glacial ice and the background (i.e. sea ice). So, the increase can be associated with the sea ice extension cycle, with a minimum in summer and maximum in winter (Parkinson and Cavalieri, 2012).

## 6. Discussion

In the previous sections, we have presented a novel iceberg detection adaptive machine learning method. We have focused our efforts in improving the iceberg detection performance under large image background variability, not only in terms of size but also regarding intensity and texture. The main difference to more traditional methods is that our approach is not centred on the use of predictive models based on backscatter intensity (Williams et al., 1999; Silva and Bigg, 2005; Wesche and Dierking, 2012, 2015; Frost et al., 2016; Mazur et al., 2017). Instead, we use different predictive models that are individually weak, but robust when combined together since they are all based on

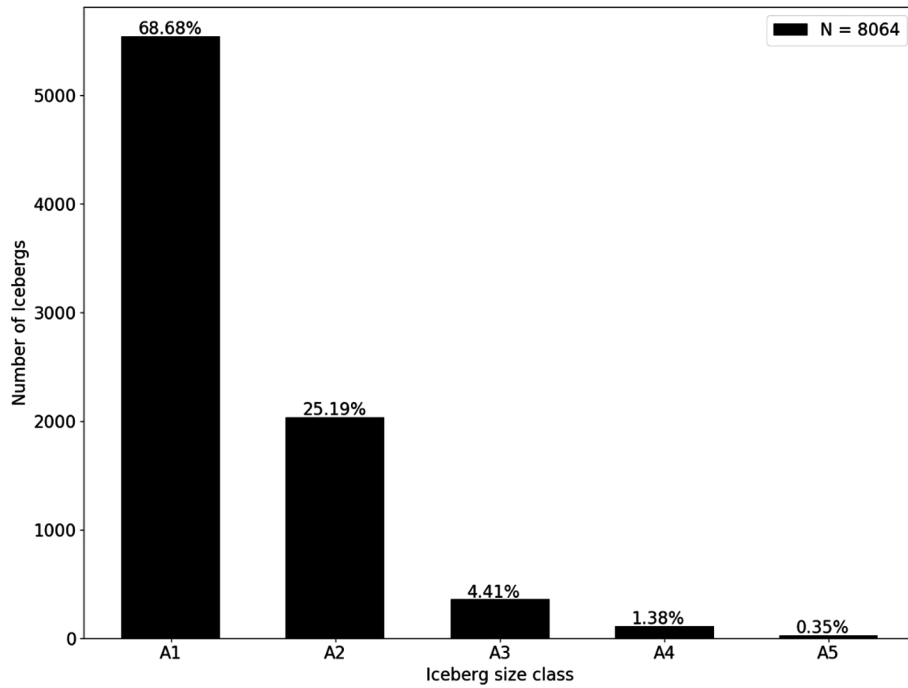


**Fig. 9.** Icebergs size class distribution, identified from RAMP AMM-1 mosaic (1997) and Envisat ASAR dataset (2003, 2004–2005). Size classes defined as A1 = 0.1–1 km<sup>2</sup>, A2 = 1–10 km<sup>2</sup>, A3 = 10–100 km<sup>2</sup>, A4 = 100–1000 km<sup>2</sup> and A5 > 1000 km<sup>2</sup>.

different ambiguous image patterns. Moreover, the method continuously receives feedback from previous detections in order to improve the detection over targets with patterns that were not previously seen by the predictors.

In general, the ensemble/incremental learning method – more specifically, the proposed RF Committee, shows noteworthy performance improvements for ambiguous and outlier samples compared with models based on standard features that have been used to separate

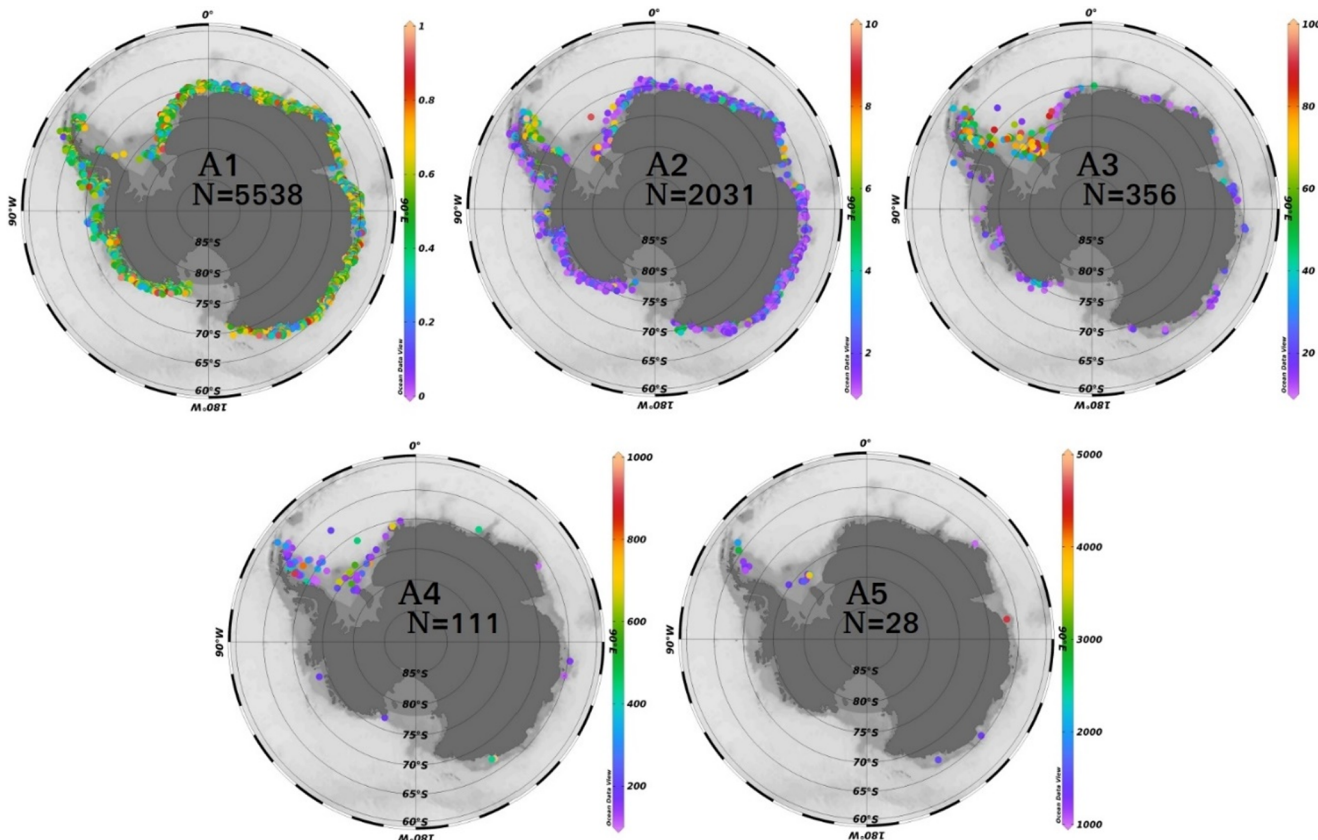


**Fig. 10.** Spatial distribution of icebergs around the Antarctic continent identified from RAMP AMM-1 mosaic (1997) and Envisat ASAR dataset (2003, 2004–2005). Panels are divided by iceberg size class (Fig. 9). The colour scales represent the iceberg size in Km<sup>2</sup>.

icebergs from the background. We achieve an average detection accuracy (from machine learning evaluation and visual inspection) of  $97.5 \pm 0.6\%$ , an average false positive rate of  $2.3 \pm 0.4\%$  and an average miss rate of  $3.3 \pm 0.4\%$ , without any manual correction of the results. These results are quite good when compared to the different methods already mentioned above. For instance, Williams et al., (1999) show an accuracy of 84%, Silva and Bigg (2005) achieved an accuracy of 70% and Wesche and Dierking (2015) show an average accuracy of 77%, whereas icebergs smaller than  $5 \text{ km}^2$  are detected with an accuracy of only 46%. In recent studies, Frost et al. (2016) show an average accuracy of 90%, while Mazur et al. (2017) achieve an accuracy of 96.2%, 3.8% misses and 7% of false positives. However, we must point out that each of the method methods mentioned above was based on different on types of SAR data (e.g. ERS, Envisat, Sentinel, TerraSAR and RadarSat) and distinct acquisition parameters as spatial and temporal resolution, band, polarization, incidence angle and orbit. Furthermore, each method was applied over different regions, being susceptible to regional variability and uniqueness.

However, despite of the significant detection performance archived by our novel methodology, the proposed RF committee method is sensitive to non-balanced training sets, tending to favour the most representative class. These aspects are similar to the observations by Dalponte et al. (2013), who applied Random Forests to tree species classification from hyperspectral data. In this sense, our method should be used with caution while applying it in conjunction with incremental learning for iceberg identification, since icebergs represent a large minority in occurrences when compared to the background (i.e. the scheme possibly tends to oversample background targets). Furthermore, the miss rate seems to be the major concern in our method, being strongly related to the segmentation stage. This is usually observed in scenes with the presence of clusters of icebergs partially connected by less than 20 intensity levels (greyscale) of distance and in scenes were large icebergs presented abrupt textural and spectral variability over their surfaces. In these situations, icebergs clusters were aggregated in single segments resulting in an over segmentation or yet a poorly defined segmentation. Although segmentation faults are not entirely explored in this study, the segmentation is an important stage to bounding icebergs and was discussed in detail by Williams et al. (1999) and Mazur et al. (2017).

Finally, although the proposed method has been developed and validated for Antarctic conditions, where the presence of tabular icebergs is the dominant feature, we believe that the adaptive method presented here can achieve satisfactory performance also for the Arctic environment. In that area, the icebergs are less tabular, often in stormy seas and/or wrapped by packs of ice with different characteristics when compared to Antarctica.

## 7. Conclusions

Automatic iceberg detection from SAR images is a challenging task. The icebergs have wide spectral signature, texture, morphology and size variability, due to a broad range of environmental conditions, impose ambiguous classification scenarios. The ambiguity between the different classification targets makes it difficult to establish an accurate predictive model, normally requiring extensive manual inspection to remove false positives and to include missing targets. This hampers extensive iceberg detection using SAR imagery, which is essential for operational applications and studies on iceberg distribution patterns as well as their role in the input of freshwater into the ocean and therefore in the climate.

## Appendix A. Features description

- Frequency texture features based on Gabor filter:

Gabor wavelet can be applied locally resulting in a Gabor filtered image. When applying a Gabor filter to the original image, the content is broke

The method introduced in this study is an alternative machine learning approach, which employs an adaptive solution to extensive automatic iceberg identification from SAR images. We show that the ambiguity between icebergs and background can be bypassed by improving the generalization through a gradual learning information flow and the combination of heterogenous predictive models. The iceberg detection method uses a superpixel segmentation (Graph-based), ensemble learning (Random Forest Committee) and incremental learning (Batch learning).

The proposed method is robust detecting Antarctic icebergs with areas between  $0.1$  and  $4567.82 \text{ km}^2$ . The graph-based superpixel segmentation algorithm was capable to produce solid and well-defined segmentation, providing a convenient basis to compute image features and estimate iceberg spatial properties. The ensemble/incremental strategy resulted in an average accuracy, false positive rate and miss rate of  $97.5 \pm 0.6\%$ ,  $2.3 \pm 0.4\%$  and  $3.3 \pm 0.4\%$ , respectively. The high performance is attributed to the strong generalization achieved by the combination of heterogeneous predictive models. Each model has a unique view of the differences between icebergs and background, based on different image features. Moreover, the continuously dynamic addition of new samples to the predictive models has a strong positive influence on the performance of the iceberg detection.

Finally, our method has the potential to contribute to oceanographic and cryospheric research by offering a suitable and robust approach focused on the improvement of detecting icebergs under wide range of scenarios in digital SAR images. Operationally, the proposed method fixes the problem of detecting icebergs under large radar backscattering variability. Moreover, our results clearly demonstrate that the error in separating icebergs from their surrounding can be reduced by combining heterogeneous predictive models, which are incrementally improved to adjust to outliers. Altogether, our results highlight the potential of machine learning approaches for remote sensing applications where highly ambiguous scenarios pose as major obstacles for classification and analysis. The detection method presented here has been recently used to compute the pan-Antarctic near-coastal iceberg distribution complementing previous studies restricted to open-water regions (Barbat et al., 2019). Moreover, this technique can be used as basis for future drifting iceberg studies that would throw light on the patterns of freshwater input from icebergs in the Southern Ocean.

## Acknowledgments

This study is a contribution to the activities of the Brazilian High Latitudes Oceanography Group (GOAL) and the Brazilian National Institute of Science and Technology of the Cryosphere (INCT-CRIOSFERA; CNPq 465680/2014-3, FAPERGS 17/2551-0000518-0). The GOAL has been funded by the Brazilian Antarctic Program (PROANTAR) through the Brazilian Ministry of the Environment (MMA), the Brazilian Ministry of Science, Technology, Innovation and Communication (MCTIC), the Council for Research and Scientific Development of Brazil (CNPq; 442628/2018-8), and CAPES Foundation (AUXPE 1995/2014). M. M. Barbat acknowledges the fellowships from CNPq (140910/2016-6) and CAPES Foundation (88881.177236/2018-01). M. M. Mata acknowledges CNPq grant 306896/2015-0. We also thank the European Space Agency (ESA) and the Canadian Cryospheric Information Network (CCIN) for providing the Envisat ASAR images and the RAMP AMM-1 mosaic used in this study. In addition, we have uploaded the source-code for the presented method to the institutional website of Federal University of Rio Grande, Brazil at <https://goal.furg.br/producao-cientifica/supplements/202-b2019-icedt-repository>.

down in different scales and orientations that can be effectively used for pattern recognition (Ismail et al., 2014). The formal definition of Gabor filter is given as follows:

$$g(x, y) = \frac{1}{2\pi\sigma_x\sigma_y} \exp\left(-\frac{x^2}{2\sigma_x^2} - \frac{y^2}{2\sigma_y^2}\right) \exp(j\omega x) \quad (\text{A1})$$

where  $x, y$  are pixel coordinates,  $j = \sqrt{-1}$ , and  $\omega$  is frequency.

The mean and variance are computed from the filtered image.

- Texture features based on Gray-Level Co-Occurrence Matrix (GLCM) (Haralick et al., 1973), which is defined as follows:

The element point  $p(i, j)$  in GLCM represents the frequency of two pixels in a certain grayscale image window, and the adjacent distance is  $d$  in the  $\theta$  direction. Usually,  $d$  takes 1 or 2, and  $\theta$  take four directions  $0^\circ, 45^\circ, 90^\circ$  and  $135^\circ$ . Each element values of GLCM are then computed as follows:

$$p(i, j) = \frac{p(i, j, d, \theta)}{\sum_{i=1}^N \sum_{j=1}^N p(i, j, d, \theta)} \quad (\text{A2})$$

The Haralick texture features used in our method are computed for each direction as follows:

$$\text{Contrast: } \sum_{i=1}^N \sum_{j=1}^N (i - j)^2 p(i, j) \quad (\text{A3})$$

$$\text{Homogeneity: } \sum_{i=1}^N \sum_{j=1}^N \frac{p(i, j)}{1 + (i - j)^2} \quad (\text{A4})$$

$$\text{Dissimilarity: } \sum_{i=1}^N \sum_{j=1}^N |i - j| \cdot p(i, j) \quad (\text{A5})$$

- Morphological features are based on object shape, defined as follows:

$$\text{Eccentricity: } \sqrt{1 - \frac{b^2}{a^2}} \quad (\text{A6})$$

where  $a$  is the length of the major axis and  $b$  is the length of the minor axis.

Defining the convex hull as the minimum convex polygon that can enclose an image object geometry:

$$\text{Roundness: } \frac{4\pi \text{area}}{(\text{convex hull perimeter})^2} \quad (\text{A7})$$

where  $\text{convexperimeter}$  is the perimeter of the convex hull that encloses the object.

$$\text{Solidity: } \frac{\text{area}}{\text{convex hull area}} \quad (\text{A8})$$

where  $\text{convexarea}$  is the area of the convex hull that encloses the object.

$$\text{Polsby – Popper test: } \frac{4\pi A_o}{P_o^2} \quad (\text{A9})$$

where  $A_o$  is the object area and  $P_o$  is the object perimeter. A score of 1 indicates maximal compactness.

$$\text{Normalized perimeter index: } \frac{2\sqrt{\pi \text{area}}}{\text{perimeter}} \quad (\text{A10})$$

$$\text{Fractal dimension: } \frac{\log r}{\log s} \quad (\text{A11})$$

where  $r$  is the number of self-similar pieces, each scaled down by a factor  $s$ .

## References

- Achanta, R., Shaji, A., Smith, K., Lucchi, A., Fua, P., Susstrunk, S., 2010. SLIC Superpixels. EPFL Tech. Rep. 149300 15. <https://doi.org/10.1109/TPAMI.2012.120>.
- Achanta, R., Shaji, A., Smith, K., Lucchi, A., Fua, P., Sasstrunk, S., 2011. SLIC Superpixels compared to state-of-the-art superpixel methods. Pattern Anal. Mach. Intell. IEEE Trans. 34, 2274–2282. <https://doi.org/10.1109/tpami.2012.120>.
- Barbat, M.M., Rackow, T., Wesche, C., Hellmer, H.H., Mata, M.M., 2019. Three years of near-coastal Antarctic iceberg distribution from a machine-learning approach applied to SAR imagery. J. Geophys. Res. Ocean doi:10.1029/2019JC015205.
- Frost, A., Ressel, R., Lehner, S., 2016. Automated iceberg detection using high resolution X - band SAR images. Can. J. Remote Sens. 42, 354–366.
- Bigg, G.R., Wadley, M.R., Stevens, D.P., Johnson, J.A., Science, C.R., Bigg, G.R., Wadley, M.R., Stevens, D.P., Johnson, J.A., 1997. Modelling the dynamics and thermodynamics of icebergs. Cold Reg. Sci. Technol. 26, 113–135. [https://doi.org/10.1016/S0165-232X\(97\)00012-8](https://doi.org/10.1016/S0165-232X(97)00012-8).
- Beard, K.H., 2007. Random forests for classification in ecology. Ecology 88, 2783–2792. <https://doi.org/10.1890/07-0539.1>.
- Belgiu, M., Dragu, L., 2016. Random forest in remote sensing: a review of applications and future directions. ISPRS J. Photogramm. Remote Sens. 114, 24–31. <https://doi.org/10.1016/j.isprsjprs.2016.01.011>.
- Blachnik, M., Laaksonen, J., 2008. Image classification by histogram features created with learning vector quantization. Lect. Notes Comput. Sci. (including Subser. Lect. Notes Artif. Intell. Lect. Notes Bioinformatics) 5163 LNCS, 827–836. [https://doi.org/10.1007/978-3-540-87536-9\\_85](https://doi.org/10.1007/978-3-540-87536-9_85).
- Bouhier, N., Tournadre, J., Rémy, F., Gourves-Cousin, R., 2018. Melting and fragmentation laws from the evolution of two large Southern Ocean icebergs estimated from satellite data. Cryosphere 12, 2267–2285. <https://doi.org/10.5194/tc-12-2267-2018>.
- Breiman, L., 2001. Random forests. Mach. Learn. 45, 5–32. <https://doi.org/10.1023/A:1010933404324>.
- Chen, J., Pappas, T.N., Mojsilovic, A., Rogowitz, B.E., 2003. Perceptual color and spatial

- texture features for segmentation. *Hum. Vis. Electron. Imaging VIII SPIE-5007*, 340–351. <https://doi.org/10.1117/12.485528>.
- Comaniciu, D., Meer, P., 2002. Mean Shift: a robust approach towards feature space analysis. *IEEE Trans. n PAMI* 24 (5), 603–619.
- Dalponte, M., Orka, H.O., Gobakken, T., Gianelle, D., Naesset, E., 2013. Tree species classification in boreal forests with hyperspectral data. *IEEE Trans. Geosci. Remote Sens.* 51, 2632–2645.
- De Keersmaecker, M.-L., Pierre, F., Isabelle, T., 2003. Using fractal dimensions for characterizing intra-urban diversity: the example of Brussels. *Geogr. Anal.* 35, 310–328.
- Dietterich, T.G., 2000. Ensemble methods in machine learning. *Mult. Classif. Syst.* 1857, 1–15. <https://doi.org/10.1007/3-540-45014-9>.
- Du, P., Samat, A., Waske, B., Liu, S., Li, Z., 2015. Random forest and rotation forest for fully polarized SAR image classification using polarimetric and spatial features. *ISPRS J. Photogramm. Remote Sens.* 105, 38–53. <https://doi.org/10.1016/j.isprsjprs.2015.03.002>.
- Eibl, G., Pfeiffer, K.P., 2005. Multiclass boosting for weak classifiers. *J. Mach. Learn. Res.* 6, 189–210.
- ESA. European Space Agency, 2007. Envisat ASAR Product Handbook, 564.
- Felzenszwalb, P., Huttenlocher, D., 2004. Efficient graph-based image segmentation. *Int. J. Comput. Vision (IJCV)* 59 (2), 167–181.
- Gislason, P.O., Benediktsson, J.A., Sveinsson, J.R., 2006. Random forests for land cover classification. *Pattern Recognit. Lett.* 27, 294–300. <https://doi.org/10.1016/j.patrec.2005.08.011>.
- Ghosh, A., Sharma, R., Joshi, P.K., 2014. Random forest classification of urban landscape using Landsat archive and ancillary data: combining seasonal maps with decision level fusion. *Appl. Geogr.* 48, 31–41. <https://doi.org/10.1016/j.apgeog.2014.01.003>.
- Gladstone, R.M., Bigg, G.R., Nicholls, K.W., 2001. Iceberg trajectory modeling and meltwater injection in the Southern Ocean. *J. Geophys. Res.* 106, 19903–19915. <https://doi.org/10.1029/2000JC000347>.
- Gladstone, R., Bigg, G.R., 2002. Satellite tracking of icebergs in the Weddell Sea. *Antarct. Sci.* 14, 278–287. <https://doi.org/10.1017/S0954102002000032>.
- Hall, M., 1999. Correlation-based Feature Selection for Machine Learning. Waikato Univ. <https://doi.org/10.1.1.149.384>.
- Haralick, R.M., Shanmugam, K.I.D., 1973. Textural features for image classification. *IEEE Trans. Syst. Man Cybern.* 6, 610–621.
- Hayes, M., Koo, J., Cho, Y., 2014. Tracking based on Template matching with Online Random Forests.
- Impoco, G., Tuminello, L., 2015. Incremental learning to segment micrographs. *Comput. Vis. Image Underst.* 140, 144–152. <https://doi.org/10.1016/j.cviu.2015.03.007>.
- Ismail, A.S., Gao, X., Deng, C., 2014. Sar image classification based on texture feature fusion. *IEEE Trans. Geosci. Remote Sens.*
- Jacka, T.H., Giles, A.B., 2007. Antarctic iceberg distribution and dissolution from ship-based observations. *J. Glaciol.* 53, 341–356. <https://doi.org/10.3189/002214307783258521>.
- Jackson, C.R., Apel, J.R., 2005. Synthetic aperture radar marine user's manual. National Oceanic and Atmospheric Administration US Department of Commerce, Washington, DC.
- Jansen, D., Schodlok, M., Rack, W., 2007. Basal melting of A-38B: A physical model constrained by satellite observations. *Remote Sens. Environ.* 111, 195–203. <https://doi.org/10.1016/j.rse.2007.03.022>.
- Jezeck, K.C., Sohn, H.G., Noltmier, K.F., 1998. The RADARSAT Antarctic Mapping Project. IGARSS '98. Sens. Manag. Environ. 1998 IEEE Int. Geosci. Remote Sensing Symp. Proceedings. (Cat. No. 98CH36174) 2462–2464 vol.5. <https://doi.org/10.1109/IGARSS.1998.702246>.
- Lee, J.S., 1981. Speckle analysis and smoothing of synthetic aperture radar images. *Comput. Graph. Image Process.* 17, 24–32.
- Lee, J. Sen, 1983. Digital image smoothing and the sigma filter. *Comput. Vision Graph. Image Process.* 24, 255–269. [https://doi.org/10.1016/0734-189X\(83\)90047-6](https://doi.org/10.1016/0734-189X(83)90047-6).
- Marino, A., Dierking, W., Wesche, C., 2016. A Depolarization ratio anomaly detector to identify icebergs in sea ice using dual-polarization SAR images. *IEEE Trans. Geosci. Remote Sens.* 54, 5602–5615. <https://doi.org/10.1109/TGRS.2016.2569450>.
- Marino, A., Rulli, R., Wesche, C., Hajnsek, I., 2015. A new algorithm for iceberg detection with dual-polarimetric SAR data. In: *Int. Geosci. Remote Sens. Symp.* 2015-Novem, pp. 3446–3449. <https://doi.org/10.1109/IGARSS.2015.7326561>.
- Masotti, M., Campanini, R., 2008. Texture classification using invariant ranklet features. *Pattern Recognit. Lett.* 29, 1980–1986. <https://doi.org/10.1016/j.patrec.2008.06.017>.
- Mazur, A.K., Wählén, A.K., Krężel, A., 2017. An object-based SAR image iceberg detection algorithm applied to the Amundsen Sea. *Remote Sens. Environ.* 189, 67–83. <https://doi.org/10.1016/j.rse.2016.11.013>.
- Mishra, P., Chatterjee, R., Mahapatra, V., 2010. Texture Segmentation Using Gabor Filters and Wavelets.
- Muckenhuber, S., Korosov, A.A., Sandven, S., 2016. Open-source feature-tracking algorithm for sea ice drift retrieval from Sentinel-1 SAR imagery. *Cryosphere* 10, 913–925. <https://doi.org/10.5194/tc-10-913-2016>.
- Özçift, A., 2011. Random forests ensemble classifier trained with data resampling strategy to improve cardiac arrhythmia diagnosis. *Comput. Biol. Med.* 41, 265–271. <https://doi.org/10.1016/j.combiomed.2011.03.001>.
- Parkinson, C.L., Cavalieri, D.J., 2012. Antarctic sea ice variability and trends, 1979–2010. *Cryosphere* 6, 871–880. <https://doi.org/10.5194/tc-6-871-2012>.
- Perrone, M., Cooper, L., 1993. Improving regression estimation: Averaging methods for variance reduction with extensions to general convex measure optimization.
- Polikar, R., 2006. Ensemble based systems in decision making. *Circuits Syst. Mag. IEEE* 6, 21–45. <https://doi.org/10.1109/MCAS.2006.1688199>.
- Polsby, D.D., Popper, R.D., 1991. The Third Criterion: Compactness as a procedural Safeguard Against Partisan Gerrymandering. *Yale L. & Pol'Y Rev.* 9, 2. <https://digitalcommons.law.yale.edu/ylpr/vol9/iss2/6>.
- Puissant, A., Rougier, S., Stumpf, A., 2014. Object-oriented mapping of urban trees using Random Forest classifiers. *Int. J. Appl. Earth Obs. Geoinf.* 26, 235–245. <https://doi.org/10.1016/j.jag.2013.07.002>.
- Romanov, Y.A., Romanova, N.A., Romanov, P., 2012. Shape and size of Antarctic icebergs derived from ship observation data. *Antarct. Sci.* 24, 77–87. <https://doi.org/10.1017/S0954102011000538>.
- Romanov, Y.A., Romanova, N.A., Romanov, P., 2008. Distribution of icebergs in the Atlantic and Indian ocean sectors of the Antarctic region and its possible links with ENSO. *Geophys. Res. Lett.* 35. <https://doi.org/10.1029/2007GL031685>.
- Rosich, B., Meadows, P., 2004. Absolute Calibration of ASAR Level 1 Products Generated with PF-ASAR.
- Schodlok, M.P., Hellmer, H.H., Rohardt, G., Fahrbach, E., 2006. Weddell Sea iceberg drift: five years of observations. *J. Geophys. Res. Ocean.* 111, 1–14. <https://doi.org/10.1029/2004JC002661>.
- Silva, T.A.M., Bigg, G.R., 2005. Computer-based identification and tracking of Antarctic icebergs in SAR images. *Remote Sens. Environ.* 94, 287–297. <https://doi.org/10.1016/j.rse.2004.10.002>.
- Silva, T.A.M., Bigg, G.R., Nicholls, K.W., 2006. Contribution of giant icebergs to the Southern Ocean freshwater flux. *J. Geophys. Res. Ocean.* 111. <https://doi.org/10.1029/2004JC002843>.
- Singh, M., Singh, S., 2002. Spatial texture analysis: a comparative study. In: *Proc. 16th Int. Conf. Pattern Recognit.*
- Shaw, T.J., Raiswell, R., Hexel, C.R., Vu, H.P., Moore, W.S., Dudgeon, R., Smith, K.L., 2011. Input, composition, and potential impact of terrigenous material from free-drifting icebergs in the Weddell Sea. *Deep Res. Part II Top. Stud. Oceanogr.* 58, 1376–1383. <https://doi.org/10.1016/j.dsr2.2010.11.012>.
- Schwarz, J.N., Schodlok, M.P., 2009. Impact of drifting icebergs on surface phytoplankton biomass in the Southern Ocean: ocean colour remote sensing and in situ iceberg tracking. *Deep Res. Part I Oceanogr. Res. Pap.* 56, 1727–1741. <https://doi.org/10.1016/j.dsr.2009.05.003>.
- Stern, A.A., Adcroft, A., Sergienko, O., 2016. The effects of Antarctic iceberg calving-size distribution in a global climate model. *J. Geophys. Res. Ocean.* 121, 5773–5788. <https://doi.org/10.1002/2016JC011835>.
- Tremeau, A., Colantoni, P., 2000. Regions adjacency graph applied to color image segmentation. *IEEE Trans. Image Process.* 9 (4), 735–744.
- Veldadi, A. and Soatto, S. 2008. Quick Shift and kernel methods for mode seeking. In: *Proc. of ECCV*, pp. 705–718.
- Wesche, C., Dierking, W., 2012. Iceberg signatures and detection in SAR images in two test regions of the Weddell Sea, Antarctica. *J. Glaciol.* 58, 325–339. <https://doi.org/10.3189/2012J0G11J020>.
- Wesche, C., Dierking, W., 2015. Near-coastal circum-Antarctic iceberg size distributions determined from Synthetic Aperture Radar images. *Remote Sens. Environ.* 156, 561–569. <https://doi.org/10.1016/j.rse.2014.10.025>.
- Williams, R.N., Rees, W.G., Young, N.W., 1999. A technique for the identification and analysis of icebergs in synthetic aperture radar images of Antarctica. *Int. J. Remote Sens.*
- Zhang, Q., Liu, Y., Zhu, S., Han, J., 2017. Salient object detection based on super-pixel clustering and unified low-rank representation. *Comput. Vis. Image Underst.* 161, 51–64. <https://doi.org/10.1016/j.cviu.2017.04.015>.
- Zhou, Z.-H., 2012. Ensemble Methods Foundations and Algorithms, Machine Learning & Pattern Recognition Series.